



Shock-cell spacings of underexpanded sonic jets emerging from elliptic nozzles

Tatsuya Nagata¹ · Muhammad Minarul Islam^{1,2} · Takeshi Miyaguni¹ · Shinichiro Nakao¹ · Yoshiaki Miyazato¹

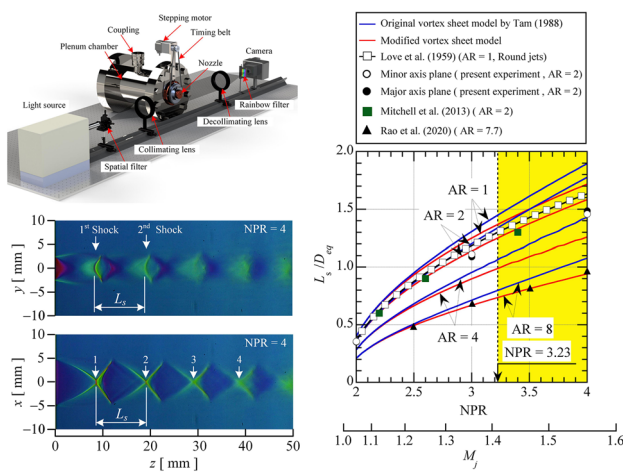
Received: 7 February 2022 / Revised: 18 May 2022 / Accepted: 31 May 2022

© The Author(s), under exclusive licence to Springer-Verlag GmbH Germany, part of Springer Nature 2022

Abstract

The shock-cell structures of underexpanded sonic jets emerging from an elliptic convergent nozzle with an aspect ratio of 2 at the exit are investigated using rainbow schlieren deflectometry. A rainbow filter with fine color gradations is placed perpendicular to the nozzle axis in the schlieren cut-off plane. Experiments are performed under a nozzle pressure ratio (NPR) of 2.0, 3.0, and 4.0; the NPR can be defined as the ratio of the stagnation pressure upstream of the nozzle to the back pressure. The flow features of the jet major and minor axis plane views are demonstrated with hue variations approximately proportional to the streamwise density gradients in the jets. In addition, the shock-cell spacings of elliptic underexpanded sonic jets are obtained for various NPRs and compared quantitatively with an approximate solution using the modified vortex sheet model, where the characteristic length of the fully expanded jet is redefined from the original model proposed in a previous study. Furthermore, the effects of the aspect ratio at the nozzle exit on the shock-cell spacing are elucidated through a quantitative comparison between the experiment and model.

Graphical abstract



M. M. Islam, T. Miyaguni, S. Nakao and Y. Miyazato have contributed equally to this work.

✉ Yoshiaki Miyazato
miyazato@kitakyu-u.ac.jp

Tatsuya Nagata
d2mba017@eng.kitakyu-u.ac.jp

Muhammad Minarul Islam
minarul_math@bsmrstu.edu.bd

Takeshi Miyaguni
t-miyaguni@kitakyu-u.ac.jp

Shinichiro Nakao
s-nakao@kitakyu-u.ac.jp

¹ Department of Mechanical Systems Engineering, The University of Kitakyushu, 1-1 Hibikino, Wakamatsu-ku, Kitakyushu 808-0135, Japan

² Department of Mathematics, Bangabandhu Sheikh Mujib Rahman Science and Technology University, Gopalganj 8100, Bangladesh

1 Introduction

Although numerous studies have been conducted on supersonic jets emerging from circular nozzles Franquet et al. (2015), to the best of our knowledge, only a few studies have performed experiments on those emerging from elliptic nozzles. Elliptic supersonic jets are a promising tool for effective mixing in air-breathing engines to enhance the efficiency of the vehicle Ihme (Ihme 2017). Elliptic jets under off-design conditions produce intricate shock systems in the jet plume, resulting in an intense tone, referred to as screech Edgington-Mitchell (2019), which plays a critical role in the design of advanced aircraft because it can cause sonic fatigue failure. However, the internal shock structures in shock-containing elliptic jets have not been examined sufficiently owing to a challenging issue.

Kinzie and McLaughlin (1999) experimentally investigated the aerodynamic and acoustic properties of shock-free supersonic jets emerging from elliptic and circular nozzles with a design Mach number of approximately 1.5. They found that elliptic jets radiate less noise than their corresponding round jets. Menon and Skews (2010) performed extensive research on shock wave configurations and flow structures in underexpanded sonic jets emerging from non-axisymmetric nozzles, including rectangular, elliptical, and slot nozzles. For elliptic underexpanded jets, they experimentally and numerically found that the incident shock generated near the nozzle exit is not formed along the minor axis plane of the nozzle for aspect ratios (ARs) larger than 2. Instead, it originates downstream from the nozzle exit in the major axis plane. The flow characteristics of underexpanded jets from an elliptic nozzle with a design Mach number and AR of 2 each at the nozzle exit were investigated experimentally by Kumar and Rathakrishnan (2016); they conducted a Pitot probe survey and shadowgraph visualization to demonstrate the streamwise evolution of elliptic jets, such as the axis-switching phenomena. However, traditional intrusive measuring probes, such as the Pitot tube and hot-wire anemometry, are obstructed by flow intrusion and signal interpretation problems in shock-containing flows. Moreover, the determination of flow properties for a large number of spatial points using intrusive probes requires significant effort.

In contrast, Yoon and Lee (2003) used stereoscopic particle image velocimetry to investigate the near-field structure of an underexpanded jet emerging from a sharp-edged elliptic orifice with an AR of 2. Mitchell et al. (2013) and Edgington-Mitchell et al. (2015) applied high-resolution planar particle image velocimetry to a screeching underexpanded jet issuing from an elliptic nozzle, with an AR of 2, to extract information about the velocity fields and turbulent statics. However, particle-based optical methods

suffer from inadequate seeding and velocity slip errors just behind the shocks (Sakurai et al. 2015; Wernet 2016; Yüceil (2017)).

Traditionally, the conventional schlieren and shadowgraph optical techniques (Settles 2001) provide simple tools to qualitatively investigate the characteristics of shock-dominated flows. Therefore, the primary sources of experimental methods for elliptic supersonic jets include flow visualizations using schlieren Edgington-Mitchell et al. (2015) or shadowgraph Menon and Skews (2010) techniques. Recently, Rao et al. (2020) utilized time-resolved schlieren imaging with near-field acoustic measurements to investigate the screech characteristics of an underexpanded elliptic jet with a high AR of 7.72. Although the schlieren technique with a knife edge only presents the qualitative flow features, rainbow schlieren deflectometry, wherein the knife edge is replaced with a rainbow filter Agrawal and Wanstall (2018), can be used to qualitatively and quantitatively obtain the internal structures of shocks.

In this study, we focus on the shock-cell spacings of underexpanded jets emerging from elliptic nozzles because they are significantly related to the screech frequency. The shock-cell spacings are acquired quantitatively from rainbow schlieren images, which demonstrate the streamwise density gradients along the central axis of the jet. Tam (1988) proposed a vortex sheet model to investigate the shock-cell structures of elliptic supersonic jets; however, the validity of the model could not be proved. Additionally, the model includes the disadvantage wherein the analytical solution of an elliptic jet does not match that of a round jet when the AR approaches unity. Therefore, we improve the original model to clarify this inconsistency. Furthermore, we perform quantitative comparisons between the modified model and experiments to investigate the effects of the AR and nozzle pressure ratio (NPR) on the shock-cell spacings.

2 Experimental setup

The experiments were conducted in a blowdown compressed-air facility in the High-Speed Gasdynamics Laboratory at the University of Kitakyushu. Ambient air is pressurized by the compressor up to 1 MPa and stored in a high-pressure reservoir comprising two storage tanks with a total capacity of 2 m³ after filtering and drying. The supply line from the reservoir can be connected to the plenum chamber through coupling, as shown in Fig. 1. Hence, the high-pressure dry air from the reservoir gets stagnated in the plenum chamber; subsequently, it is discharged into the atmosphere through a test nozzle that can be rotated about its central axis (Takano et al. 2016). The desired NPR (p_{os}/p_b)

is achieved by changing the plenum pressure, p_{os} , because the back pressure, p_b (= atmospheric pressure), is constant.

An elliptic convergent nozzle with an AR of 2 at the nozzle exit was used as the test nozzle. The nozzle wall contour from the inlet to the exit was designed based on a sinusoidal curve to provide smooth uniform flows at the inlet and exit. The nozzle was manufactured using a 3D-printer (Flash-forge, Adventurer 3X) based on fused deposition modeling, where the melt extrusion method was used to deposit filaments of thermoplastic based on a specific pattern.

The cut model of the nozzle is shown in Fig. 2. The Cartesian coordinate system (x, y, z) is employed with its origin at the center of the nozzle exit plane; the x -, y -, and z -axes are oriented along the direction of the optical axis, vertical axis, and jet central axis, respectively. The semi-major and semi-minor axes of the nozzle inlet are 30 ± 0.05 mm and 15 ± 0.05 mm, respectively, and the corresponding ones at the nozzle exit are $L_a = 5 \pm 0.05$ mm (major radius) and $L_b = 2.5 \pm 0.05$ mm (minor radius), respectively. The axial length from the nozzle inlet to the exit is 75 mm; the nozzle has an elliptic cross section at each axial position. The wall shape at the nozzle exit section and the wall roughness inside the nozzle play an important role for the flow feature of a jet emerging from a nozzle. Hence, we obtained a digital image of the nozzle exit section by the laser scanning microscope (Olympus, LEXT OLS4100) and then measured the wall shape against the polar angle θ as shown in Fig. 3. The red line is the theoretical curve of the ellipse, and the open symbols show the measured values. Excellent quantitative agreement is reached between the theory and measurement with a standard deviation of about 22 μm . In addition, the arithmetic wall roughness, R_a , inside the nozzle was measured by the surface roughness measuring machine (Mitutoyo, SV-C524) with a resolution of 0.05 μm for vertical and horizontal directions, resulting in around 6 μm .

The jet flow fields were visualized through rail-mounted optical components, including a spatial filter with a rectangular slit of $3 \text{ mm} \times 50 \mu\text{m}$; two achromatic lenses with a diameter and focal length of 100 and 500 mm, respectively; a rainbow filter with a continuous hue variation at a width of 2.4 mm; and a digital camera (Nikon D7100, 6000×4000 square pixel resolution with a 14-bit pixel depth) fitted with a focusing lens with a diameter and focal length of 30 mm and 600 mm, respectively. A continuous 250 W metal halide light source (Sigmakoki, IMH-250) connected to a fiber optic cable with a diameter of 50 μm provides light input to the spatial filter through an objective lens of focal length 16.56 mm. The rainbow filter was introduced into the focal plane (schlieren cut-off plane) of the decollimating lens vertically with respect to the nozzle axis. This filter setting corresponds to the vertical knife edge in the conventional schlieren system.

The camera outputs of rainbow schlieren images in the RGB format were transferred onto a personal computer hard drive using the Nikon Camera Control Pro software and then stored as JPEG files. Each JPEG RGB image (8-bit each) was turned into an HSI image (8-bit each) according to the hue (H)-saturation (S)-intensity (I) representation obtained from direct transformation of the RGB tristimulus values (Greenberg et al. 1995). The hue (H) values transformed only were utilized to calculate the ray shift (d) at the cut-off plane of the schlieren system. This means that a unique hue can be transmitted to the image plane from a given location on the filter plane (Greenberg et al. 1995). Thus, the ray shift on the filter plane could be related to the hue measured in the image plane. This color representation eliminates numerous problems associated with inhomogeneous absorption or scattering of light by the medium, nonlinearities in recording the image, intensity fluctuations of the source and so on (Greenberg et al. 1995; Al-Ammar et al. 1998).

The rainbow filter was calibrated by moving the filter in the direction of the nozzle axis in intervals of 10 μm before starting the experiments. The calibration curve of the rainbow filter is shown in Fig. 4. The open symbols express the experimental data with a maximum precision error of about 1 deg on the hue values. The solid line indicates a least squares regression line of the experimental data, which is given by a fifth-order polynomial. The background hue in the rainbow filter for the present experiment corresponds to the location shown as the red arrow.

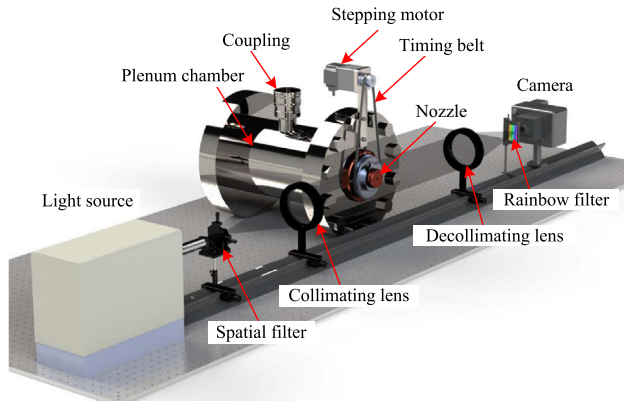


Fig. 1 Schematic of the blowdown compressed-air facility with a rainbow schlieren optical system. A test nozzle was attached to the plenum chamber with a pulley that can be rotated about its central axis using a stepping motor through a timing belt. The supply line from the reservoir can be connected to the plenum chamber through coupling. A rainbow filter was introduced into the schlieren cut-off plane just before the camera; it was set perpendicular to the flow direction, similar to the conventional vertical cut-off schlieren system

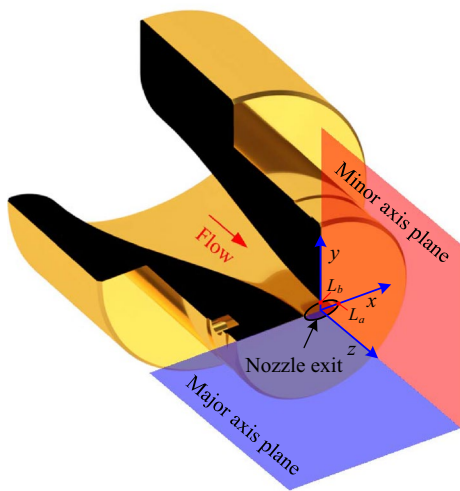


Fig. 2 Cut-model of an elliptic convergent nozzle with an AR of 2 at the exit. The Cartesian coordinate system (x,y,z) is selected, with its origin at the center of the nozzle exit plane, where the x -, y -, and z -axes are oriented along the direction of the optical axis, vertical axis, and jet central axis, respectively. The minor and major axis planes are defined as shown in the figure. The total length along the major and minor axes of the nozzle exit plane is $2L_a = 10$ mm (width) and $2L_b = 5$ mm (height), respectively, and the AR ($= L_a/L_b$) was 2

The total ray deflection angle ϵ_z in the streamwise direction (z direction) as it emerges out of the jet density field is given by

$$\epsilon_z = \frac{d}{f_d} \quad (1)$$

using geometric optics with the focal length f_d of the decollimating lens and the ray shift (d) Al-Ammar et al. (1998). Therefore, the density gradient integrated along the line-of-sight direction (called the integrated density gradient, herein) can be expressed by

$$\int_{-\infty}^{\infty} \frac{\partial \rho}{\partial z} dx \text{ or } \int_{-\infty}^{\infty} \frac{\partial \rho}{\partial z} dy = \frac{d}{K f_d} \quad (2)$$

where K is the Gladstone–Dale constant. Eventually, the integrated density gradient in the minor or major axis plane views can be derived from the hue values of the schlieren images through the filter calibration curve.

The schlieren pictures of the major and minor axis plane views were captured with an exposure time of 1/8000 s and ISO 640 with a continuous schlieren light source for a fixed NPR. The center of the jet was in focus. Five schlieren images were recorded for each NPR to estimate the statistical information such as the average, standard deviation, and so on. In this study, the shock-cell structures at the jet major and minor axis planes for an NPR of 2.0, 3.0, and 4.0, were visualized to obtain both the flow features of shock-containing elliptic

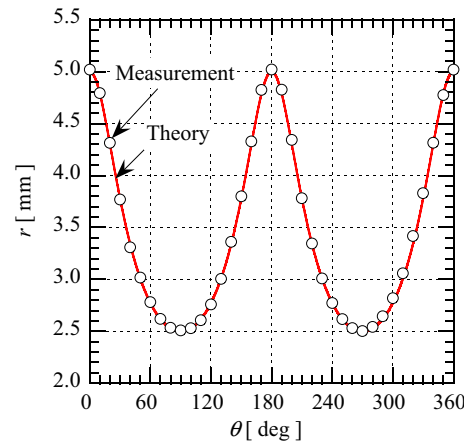


Fig. 3 Wall shape at the nozzle exit section against the polar angle. The red line denotes the theoretical curve for an ellipse with semi-major and semi-minor axes of 5 mm and 2.5 mm, respectively, and the open symbols are measured values

jets and the relationship between the shock-cell spacings and the NPR.

3 Modified vortex sheet model

Tam (1988) proposed a vortex sheet model to estimate the gross features of non-axisymmetric supersonic jets emerging from convergent-divergent nozzles operating at slightly off-design conditions, wherein a jet with arbitrary cross-sectional geometry can be modeled through eigenfunction expansion. In the model, the mixing layer of the jet is approximated by a vortex sheet and the shock-cell structure is confined to the interior of the vortex sheet. In addition, the flow is assumed to be inviscid inside the vortex sheet and there is no external disturbance.

If an elliptic jet with semi-major axis L_a and semi-minor axis L_b at the nozzle exit is fully expanded to form an ellipse jet with semi-major axis L_A and semi-minor axis L_B , the vortex sheet is characterized by a parameter μ_0 in the elliptic cylinder coordinates. The constant μ_0 curve describes an ellipse with focal length a , as shown in Fig. 5.

For a specified L_A and L_B , a and μ_0 can be expressed as

$$a = \sqrt{L_A^2 - L_B^2}, \quad \mu_0 = \tanh^{-1} \frac{L_B}{L_A} \quad (3)$$

In practical situations, L_A and L_B can be derived in advance from the definition of the characteristic length (Tam 1988) of the fully expanded jet:

$$\frac{L_A}{L_a} = \left(\sqrt{\frac{A_j}{A_d}} - 1 \right) \frac{\pi L_b}{2 L_a E(e)} + 1 \quad (4)$$

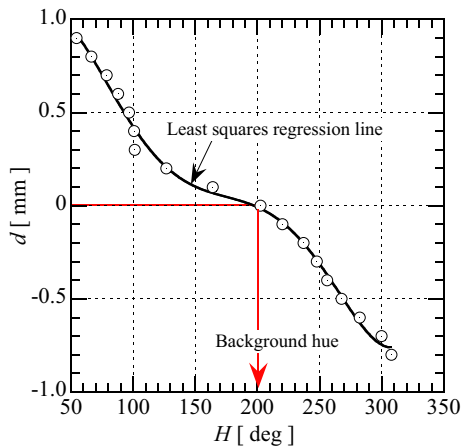


Fig. 4 Calibration characteristics of a rainbow filter. The filter calibration was performed by moving the filter at steps of $10 \mu\text{m}$ in the schlieren cut-off plane before starting experiments. The open symbols denote calibration data and a fifth-order polynomial curve fitting is utilized as least squares regression

$$\frac{L_B}{L_b} = \left(\sqrt{\frac{A_j}{A_d}} - 1 \right) \frac{\pi}{2E(e)} + 1 \quad (5)$$

where $E(e)$ is the complete elliptic integral of the second kind with eccentricity $e = (1 - L_b^2/L_a^2)^{1/2}$, which is defined as

$$E(e) = \int_0^{\frac{\pi}{2}} \sqrt{1 - e^2 \sin^2 t} dt \quad (6)$$

It should be noted that Eqs. (4) and (5) are different from those defined in Tam (1988) because $\sqrt{A_j/A_d}$ is used instead of A_j/A_d . These modified expressions yield a reasonable result, indicating that the theoretical solution for the elliptic jet is identical to that (Eq. (11) given later) obtained for a round jet as the AR, L_b/L_a , approaches unity.

The ratio A_j/A_d of the cross-sectional area of the fully expanded jet, A_j , to that of the jet at the nozzle exit, A_d , can be determined using the continuity equation between the nozzle exit and vortex sheet, as follows:

$$\frac{A_j}{A_d} = \frac{M_d}{M_j} \left[\frac{(\gamma - 1)M_j^2 + 2}{(\gamma - 1)M_d^2 + 2} \right]^{\frac{1}{2(\gamma-1)}} \quad (7)$$

where γ denotes the specific heat ratio, M_d is the nozzle design Mach number, and M_j is the fully expanded jet Mach number, which is related to NPR, as follows:

$$M_j = \sqrt{\frac{2}{\gamma - 1} \left(\text{NPR}^{\frac{\gamma-1}{\gamma}} - 1 \right)} \quad (8)$$

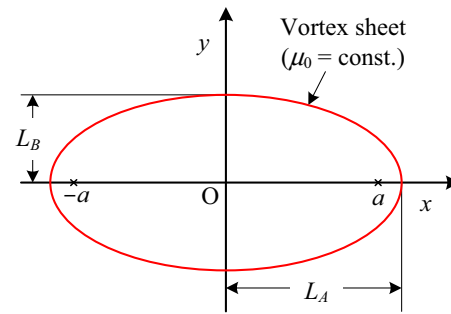


Fig. 5 Schematic of vortex sheet with the semi-major and semi-minor axes of L_A and L_B , respectively, and focal length a . The vortex sheet is characterized by a constant μ_0 curve, whose coordinates are confoal ellipses centered on the origin in the elliptic cylindrical coordinate

The perturbation conservative equations of a slightly under-expanded jet emerging from a nozzle with an elliptical cross section at the nozzle exit can be solved as an eigenvalue problem in terms of the elliptic cylinder coordinates. However, this study is not focused on the complete solutions for the pressure, density, and velocity inside the jet; instead, only the shock-cell spacing, L_s , can be given by Tam (1988):

$$L_s = \frac{\pi a \sqrt{M_j^2 - 1}}{\sqrt{q_{01}}} \quad (9)$$

where q_{01} is the smallest root of the modified Mathieu functions (McLachlan 1964) $Ce_{2n}(\mu_0, q_{nm})(n = 0, 1, 2, \dots; m = 1, 2, 3, \dots)$.

As shown in Fig. 6, a plot of $a/(L_A \sqrt{q_{01}})$ against L_B/L_A can be used to effectively estimate the shock-cell spacing, L_s , because it can be easily calculated through direct substitution into Eq. (9). An approximate solution to the theoretical curve is given by:

$$\frac{a}{L_A \sqrt{q_{01}}} = 1.285 \frac{L_B}{L_A} - 0.455 \left(\frac{L_B}{L_A} \right)^2 \quad (10)$$

It should be noted that as L_B/L_A approaches zero and unity, the corresponding values on the vertical axis converge to zero and 0.8316, respectively, which are related to the shock-cell spacing of a rectangular jet with a large AR and that of a round jet, respectively. The shock-cell spacings corresponding to both limits are

$$L_s = \frac{\pi D_e \sqrt{M_j^2 - 1}}{2.405} \sqrt{\frac{A_j}{A_d}} \quad (11)$$

for a round jet with diameter D_e at the nozzle exit and

$$L_s = 2h \frac{A_j}{A_d} \sqrt{M_j^2 - 1} \quad (12)$$

for a rectangular jet with a small dimension (height in the minor axis plane), h , at the nozzle exit. The vortex sheet model is only effective over a range of jet operating conditions, defined by

$$|M_j^2 - M_d^2| < 1 \quad (13)$$

with M_j and M_d . Beyond this range, this model generally ceases to be valid because the shock is strong or a Mach shock occurs in the jet plume.

4 Results and discussion

4.1 Shock-cell structure of underexpanded sonic jets emerging from elliptic nozzles

Figures 7 and 8 show the rainbow schlieren images of elliptic underexpanded sonic jets for three NPRs (2, 3, and 4) with the flow from left to right; the view shown in Fig. 7 (minor axis plane view) features the nozzle short dimension; the long dimension is perpendicular to the plane of the schlieren image, and vice versa for Fig. 8 (major axis plane view) where the view from the nozzle long dimension is shown. These pictures show single instantaneous images, but not time averaged ones.

The hue range is shown at the top of the figure. The hue shifts from the background hue in each schlieren image can be correlated with the deflection angle of light rays after passing the jet through the filter calibration curve, which is approximately proportional to the streamwise integrated density gradients.

No distinct variations are observed in the jet structure for Figs. 7a and 8a because the density at an NPR of 2 only changes slightly (note that the jet is ideally expanded at $NPR = 1.89$). As shown in Figs. 7b and 8b for $NPR = 3$, the violet regions exhibiting flow expansion are produced downstream of the nozzle exit, followed by the yellow regions exhibiting flow compression. The sharp concave boundaries at the end of each compression zone correspond to the termination positions of each shock in the shock cells, which are indicated by downward arrows with the 1st shock and 2nd shock in Figs. 7b and c. Such termination positions are also marked by vertical downward arrows in Figs. 8b and c, and numbered using Arabic numerals from the first shock at the nozzle exit. The L_s in Figs. 7c and 8c indicates the shock-cell spacing as a reference later.

The first two shocks can be clearly identified in Figs. 7b and c by their corresponding sharp concave lines in the jet; however, the subsequent downstream shocks are blurry

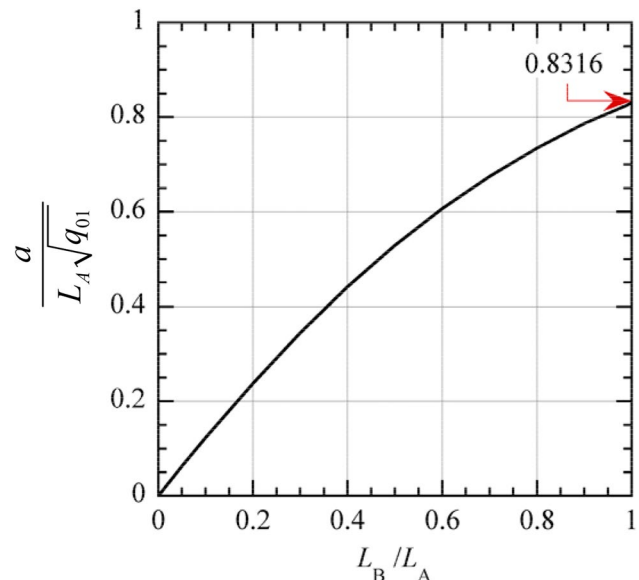


Fig. 6 Normalized parameters of the shock-cell spacings of shock-containing jets emerging from elliptic nozzles with arbitrary ARs at the exit. The limit (0.8316) of the parameter curve as L_B/L_A approaches unity can be used to estimate the theoretical shock-cell spacings of a shock-containing jet emerging from a round nozzle

owing to the flapping of the jet about the major axis (Edgington-Mitchell 2019). Mitchell et al. (2013) applied the planar particle image velocimetry to jets emerging from a convergent elliptic nozzle of $AR = 2$ for $NPR = 2.2, 2.6, 3.4$, and 4.2. They captured the jet fluctuating velocity fields, showing that the jet oscillates about the major axis for the first three NPRs and a flapping oscillation cannot be observed at $NPR = 4.2$. Unlike the concave shocks shown in Fig. 7b, Fig. 8b exhibits a Mach shock composed of an incident shock, reflected shock, and Mach stem. A comparison of Figs. 8b and c indicates that the number of shock cells and the spacing between consecutive shock cells increase with increasing NPR.

When compared to round jets, elliptic jets show the following different characteristic aspects. A strong shock (Mach stem) appears in elliptic jets for $NPR = 3$. However, Love et al. (1959) concluded from a lot of experimental data for round sonic jets that a Mach disk (it is called the Riemann shock in Love et al. (1959)) occurs when the ratio p_e/p_b of the static pressure at the nozzle exit to the back pressure exceeds about 2, which corresponds to $NPR = 3.79$. Similarly, Sugawara et al. (2021) found that a Mach disk are not produced in round jets for $NPR = 3$. As another conspicuous flow feature on elliptical jets, although incident shocks appear clearly in the major axis plane (Fig. 8c) for $NPR = 4$, they cannot be recognized in the minor axis plane (Fig. 7c). On the other hand, Sugawara et al. (2020) found

that no incident shock is present in front of a Mach disk for round sonic jets of $NPR = 4$.

Figures 9 and 10 present the streamwise hue distributions along the jet axis obtained from the corresponding rainbow schlieren images in Figs. 7 and 8; the profiles are represented with the precision error bars with the 95% confidence interval. Note that the error bars only refer to hue values, but not position errors in the streamwise direction (z direction). In addition, the experimental values include effects of flow unsteadiness. The level ($H = \text{around } 200$) of the background hue is indicated by the dashed line parallel to the abscissa in each figure. The hue distributions for an $NPR = 2$ in Figs. 9a and 10a demonstrate nearly sinusoidal waves, ranging from the nozzle exit to $z = \text{approximately } 35 \text{ mm}$; however, the hue amplitude that is directly proportional to the shock strength decreases gradually toward the downstream. In addition, the amplitude values are larger in the minor axis plane in comparison to the major axis plane because the amplitude is proportional to the density gradient integrated in the direction of line of sight. In each hue distribution, the streamwise distance between the first and second minimum values from the nozzle exit is defined as the shock-cell spacing (L_s).

The hue distributions for $NPR = 3$ in Figs. 9b and 10b exhibit quasi-periodic nonlinear wavy forms. The

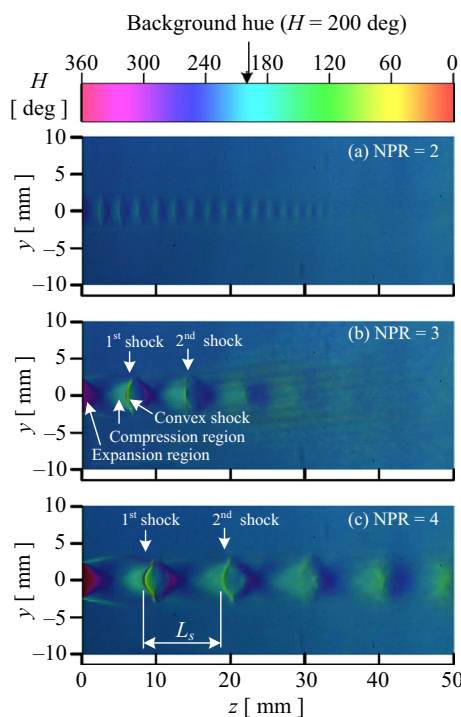


Fig. 7 Rainbow schlieren images at the minor axis plane view of elliptic underexpanded sonic jets for three $NPRs$ of 2, 3, and 4. The colors in the images exhibit one-on-one correspondence with the hue values of a rainbow filter with a background hue of $H = \text{approximately } 200$. L_s is the shock-cell spacing

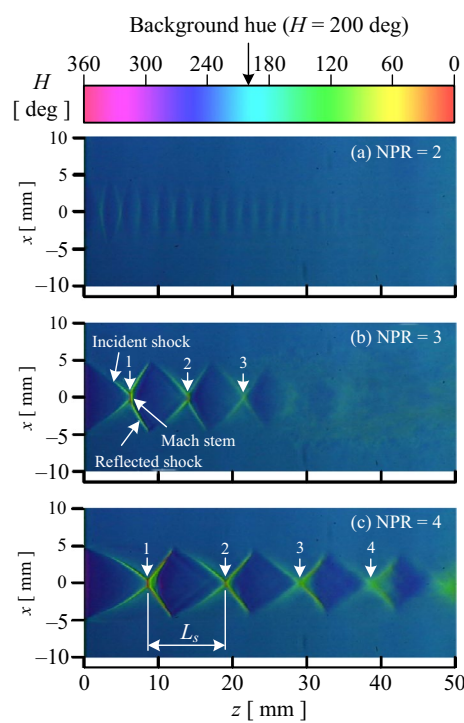


Fig. 8 Rainbow schlieren images at the major axis plane view of elliptic underexpanded sonic jets for three $NPRs$ of 2, 3, and 4. The colors of the images exhibit one-on-one correspondence with the hue values of a rainbow filter with a background hue of $H = \text{approximately } 200$. L_s is the shock-cell spacing

spacing and number of shock cells are longer and fewer than those for $NPR = 2$, respectively. The vortex sheet model implies that jets with weak shocks can be reproduced by superimposing the compression and expansion waves with some Fourier modes (Tam 1988). A distinct difference is observed in the flow properties of shock cells for an NPR of 2 and 3, which can be attributed to the wave structures, i.e., the shock-cell structure for lower $NPRs$ can be nearly reproduced by a single Fourier mode, but that for a larger NPR is given by superimposing the waves with some Fourier modes. In addition, a sudden drop followed by a sharp rise in the first shock cell of the hue distributions in Figs. 9b and 10b can be attributed to the presence of the Mach stem, as shown in Figs. 7b and 8b. Such nonlinear hue distributions can also be observed in the second shock cell. The hue amplitudes in Figs. 9b and 10b gradually decrease toward the downstream direction because the shock strength progressively diminishes from the first shock to the downstream shocks. As shown in Figs. 9c and 10c for $NPR = 4$, when the NPR increases, the hue amplitude, shock-cell spacing, and shock strength increase. A comparison of Figs. 9c and 10c for $NPR = 4$ shows that the hue distribution along the jet centerline at the minor axis plane exhibits an inverse sawtooth wave,

i.e., the wave ramps downward and then sharply rises, which is considered to be the extreme case of an asymmetric triangle wave, whereas that at the major axis plane resembles a square or pulse wave.

The distributions of the integrated density gradient along the jet centerline for $NPR = 3$ are shown in Fig. 11. The blue and red lines correspond to the distributions in the minor and major axis plane views, respectively. Shocks are given by a rapid increase in density with a positive gradient followed by a gradual decrease due to the expansion waves. The first and second shocks are represented by a sharp increase of the density gradient. It means that these shocks can be clearly seen in schlieren pictures of Figs. 7b and 8b even a 1/8000 s ($125 \mu\text{s}$) exposure time because they are considered to be spatially fixed. Since the shock is stronger upstream, the local maximum value of the integrated density gradient is larger upstream and gradually decrease toward downstream. The streamwise locations of the first and second positive peaks in the distribution (blue line) for the minor axis plane view of Fig. 11 are in good quantitative agreement with those of the first and second shocks observed by the schlieren picture of Fig. 7b. These locations also coincide with those of the first two negative peaks in Fig. 9b. Hence, the streamwise distance between the first two negative peaks in the hue distribution or the first two positive peaks in the integrated density gradient distribution is equal to the shock-cell spacing, L_s that is also shown in Figs. 7c and 8c as a reference. The same is observed in the flow properties acquired for the major axis plane view. Note that shock-cell spacings can be estimated by the hue distribution only along the jet centerline. In this situation, there is no need to make the filter calibration curve.

4.2 Shock-cell spacing

Shock-cell spacings have been commonly used to characterize shock-containing jets because of important from a fundamental and practical perspective. Although considerable effort has been devoted to the study of free jets emerging from sonic and supersonic nozzles into still air, the feature of shock-cell spacings has been poorly documented even on round sonic jets (Franquet et al. 2015). Figure 12 presents quantitative comparisons between the model and experiments for the shock-cell spacing, L_s , of underexpanded sonic jets emerging from elliptic nozzles. The equivalent diameter at the exit of an elliptic nozzle, which is given by $D_{eq} = 2(L_a L_b)^{1/2}$, is used to normalize the shock-cell spacing, L_s (Alvi et al. 1996). It is defined as the diameter of a virtual circle with the same cross-sectional area as the original circle. This length-scale for normalizing the experimental results has been successfully used to compare the data between circular and rectangular jets with equal exit areas but different geometries (Alvi et al. 1996). In addition,

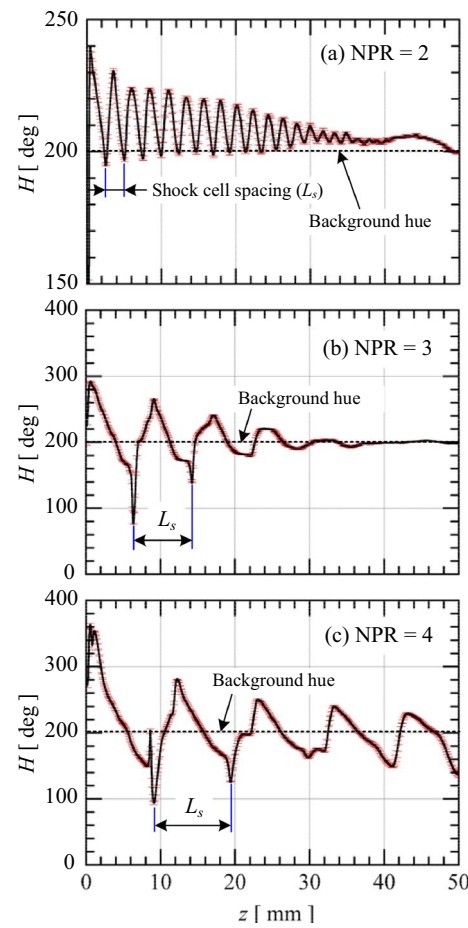


Fig. 9 Streamwise hue distributions along the jet centerline obtained from the rainbow schlieren images of the minor axis plane view. The horizontal dashed line parallel to the abscissa indicates the background hue. L_s indicates the shock-cell spacing

the fully expanded jet Mach number, M_j , given by Eq. 8 is shown with NPR in Fig. 12.

The blue and red solid lines indicate the analytical solutions calculated by the original (Tam 1988) and modified vortex sheet models, respectively. The yellow area represents the range beyond the upper limit ($NPR = 3.23$ for $\gamma = 1.4$) of the vortex sheet models, which is determined by Eqs. 8 and 13 with $M_d = 1$. It should be noted that the analytical solution calculated by the modified vortex sheet model when the AR approaches unity ($AR = 1$) coincides with that obtained from the vortex sheet model for a round jet (Eq. 11). The analytical solution obtained from the original vortex sheet model for $AR = 1$ is significantly consistent with the results calculated from the model of the corresponding round jet with the NPR ranging from 2 to approximately 2.5; however, the discrepancy increases as the NPR is increased in the range of 2.5 to 4.

It is effective to compare quantitatively the vortex sheet models with the experiments for jets emerging from round

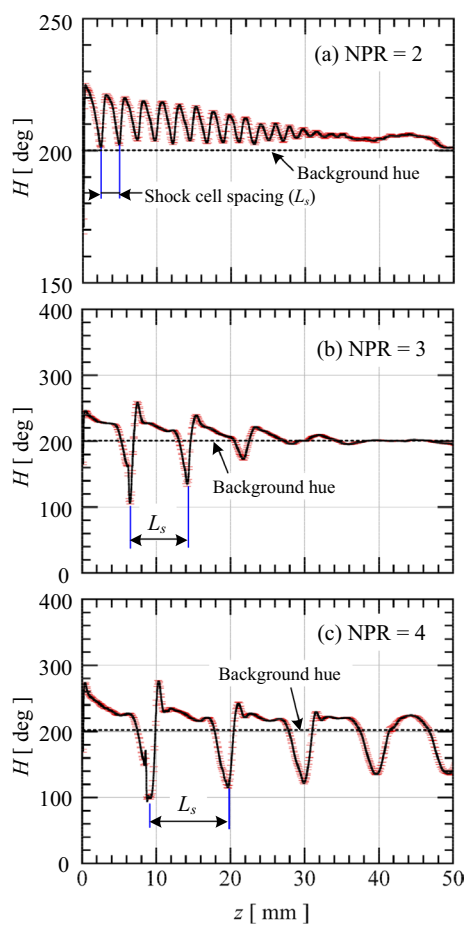


Fig. 10 Streamwise hue distributions along the jet centerline obtained from the rainbow schlieren images of the major axis plane view. The horizontal dashed line parallel to the abscissa indicates the background hue. L_s indicates the shock-cell spacing

nozzles ($AR = 1$). The black solid line with square symbols denotes the semiempirical relation for convergent round jets proposed by Love et al. (1959), which is given by

$$\frac{L_s}{D_e} = 1.55 \sqrt{0.528NPR - 1} \quad (14)$$

for $M_d = 1$ and $p_e/p_b \leq$ about 2 where D_e denotes the nozzle exit diameter. The relation was created using the shock-cell spacings determined from schlieren pictures as the distance from the nozzle exit to the point where the reflected shock intersects the jet boundary. The semiempirical relation is in good agreement with the modified vortex sheet model when compared with the original one, but both the models overestimate the semiempirical relation for larger NPR. The modified model has a deviation of around 5% at $NPR = 3.23$ when compared with the semiempirical relation.

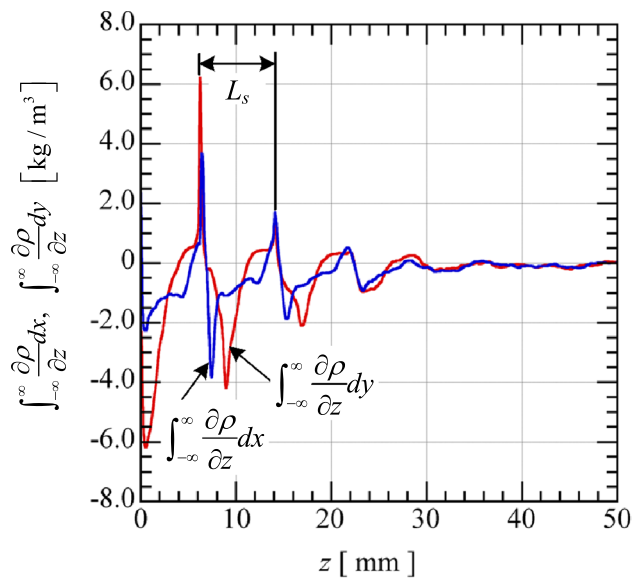


Fig. 11 Integrated density gradient distributions along the jet centerline for $NPR = 3$. The distributions corresponding to the minor and major axis plane views are shown as blue and red solid lines, respectively. Shocks are given by a rapid increase in density with a positive gradient. L_s indicates the shock-cell spacing

The open and solid circular symbols denote the experimental values obtained from the hue distributions along the jet centerlines at the minor and major axis planes, respectively. The size of the symbols is larger than the precision error in each measurement. The green square symbols show the experimental data of Mitchell et al. (2013) for $AR = 2$, which were estimated from the mean axial and transverse velocity contour maps acquired from the particle image velocimetry (PIV). The black triangular symbols depict the experimental data obtained from an elliptic convergent nozzle with an AR of 7.7, performed by Rao et al. (2020), which were reproduced in this study.

The analytical solutions from the original and modified vortex sheet models show that the normalized shock-cell spacing (L_s/D_{eq}) for a fixed AR increases with the NPR. However, for a fixed NPR, a larger AR results in a shorter L_s/D_{eq} . The modified model accords substantially with the present and Mitchell et al. (2013) experimental data for $AR = 2$, except that the model slightly overestimates the present data for $NPR = 4$. Furthermore, it also can accurately predict the experimental data of Rao et al. (2020) for $AR =$ around 8 over the entire range of NPR varying from 2.5 to 4.

It should be noted that Sugawara et al. (2020) compared free jets with a Mach disk emerging from round convergent nozzles with the exit diameters of 1 mm and 10 mm, indicating that there is almost no difference in the effects of the nozzle size on the jet centerline density profile. Furthermore, Aniskin et al. (2013) showed experimentally that the structure of shock-containing microjets emerging from

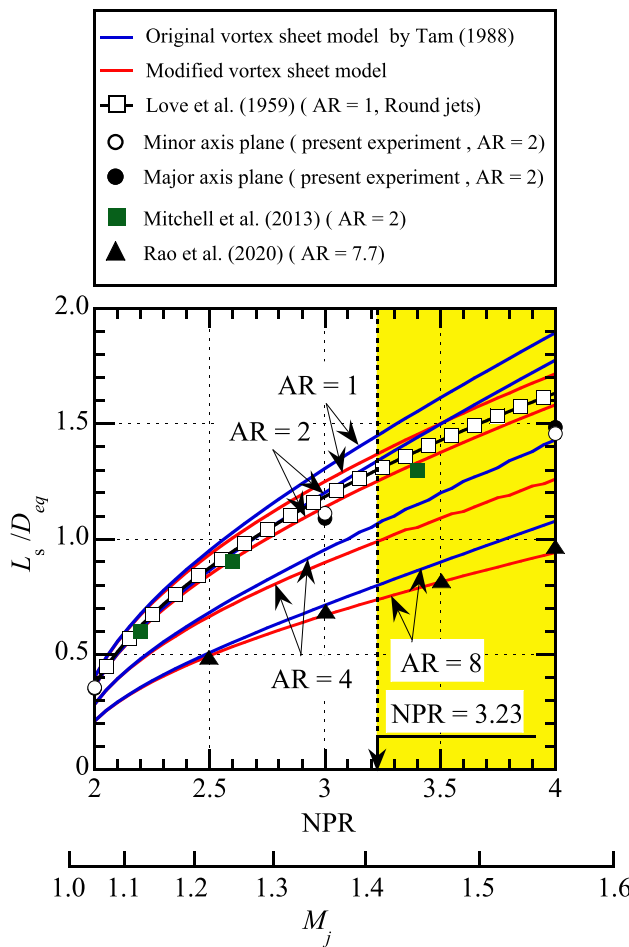


Fig. 12 Comparison between the model and experiments for the shock-cell spacings of underexpanded jets emerging from round and elliptic convergent nozzles. The shock-cell spacings are normalized by the equivalent diameter at the nozzle exit. The blue and red solid lines represent the analytical solutions calculated from the original (Tam 1988) and modified vortex sheet models, respectively. The shadow area beyond $NPR = 3.23$ indicates that it is beyond the scope of the model. The black solid line with square symbols indicates the semiempirical relation for round jets proposed by Love et al. (1959). The open and solid circular symbols represent the present experimental data obtained from the rainbow schlieren images of the minor and major axis plane views, respectively. The green square symbols are experimental data from PIV for $AR = 2$ by Mitchell et al. (2013). The black triangular symbols denote the experimental data from schlieren for $AR = 7.2$ by Rao et al. (2020), which were reproduced in this study

a convergent round nozzle with a $60 \mu\text{m}$ diameter at the exit does not differ from that of the macro-sized jets. Since an elliptic convergent nozzle with $D_{eq} = \text{around } 7 \text{ mm}$ was employed in this study, the initial shear layer thickness developing from the nozzle lip probably has no significant effect on shock-cell spacings.

5 Concluding remarks

This study presents the first stage in the investigation of the flow features of supersonic jets emerging from elliptic nozzles with various aspect ratios (ARs) at the exit. An elliptic convergent nozzle with an AR of 2 was used in this study and the semi-major and semi-minor axes of the nozzle exit face were 5 and 2.5 mm, respectively. The rainbow schlieren images of the major and minor axis plane views of the elliptic underexpanded sonic jets were captured to investigate the flow characteristics; here, a rainbow filter with a continuous hue distribution was set in the schlieren cut-off plane instead of the conventional knife edge. It was shown that a concave shock and Mach shock are observed in the first shock cell at the minor and major axis planes of the elliptic underexpanded sonic jets for higher NPRs, respectively. The hue distributions along the jet centerline were obtained from the corresponding rainbow schlieren images of the minor and major axis plane views, which were approximately proportional to the streamwise density gradient integrated along the direction of the line of sight. As a result, we found that for NPRs near the design condition of the nozzle, the hue distributions exhibit a sinusoidal variation owing to the presence of periodic weak shocks and expansion waves in the flow direction. However, in the case of moderately off-design conditions, the distribution exhibits a quasi-periodic variation with some spikes caused by Mach stems in the shock cells. The amplitudes of these distributions gradually decrease downstream because the shock strength progressively diminishes as the axial distance increases.

Shock-cell spacings were obtained experimentally from the hue distributions along the jet centerlines at the minor and major axis planes. In addition, a modified vortex sheet model was proposed to accurately predict the shock-cell spacings of underexpanded sonic jets emerging from elliptic nozzles with various ARs; in this model, the characteristic length of the original vortex sheet model was redefined to ensure that the shock-cell spacing from an elliptic nozzle is identical to that from a round nozzle as the AR approaches unity. The shock-cell spacings, normalized by the equivalent diameter, defined as the diameter of a virtual circle with the same cross-sectional area as the original one, were compared between model and experiment. The analytical solution of shock-cell spacings calculated by the modified vortex sheet model exhibits good quantitative agreement with the semiempirical relation for $AR = 1$, the present and previous experimental values for $AR = 2$, and the previous experimental values for $AR = \text{around } 8$. The modified model is superior to the original model in the estimation of shock-cell spacings, even beyond its anticipated range of validity. Furthermore, the normalized shock-cell spacing increases with increasing NPR for a constant AR; moreover, for a fixed

NPR, a larger AR results in shorter shock-cell spacing. We believe that the results presented in this paper can be used to effectively validate the computational predictions, measurement techniques, and analytical models for elliptic underexpanded sonic jets with the NPR ranging from 2 to 4.

Declarations

Conflict of interest The authors declare that they have no conflict of interest.

References

- Agrawal AK, Wanstall CT (2018) Rainbow schlieren deflectometry for scalar measurements in fluid flows. *J Flow Vis Image Process* 25:329–357
- Al-Ammar K, Agrawal AK, Gollahalli SR, Griffin D (1998) Application of rainbow schlieren deflectometry for concentration measurements in an axisymmetric helium jet. *Exp Fluids* 25:89–95
- Alvi FS, Krothapalli A, Washington D, King CJ (1996) Aeroacoustic properties of a supersonic diamond-shaped jet. *AIAA J* 34:1562–1569
- Aniskin V, Mironov S, Maslov A (2013) Investigation of the structure of supersonic nitrogen microjets. *Microfluid Nanofluidics* 14:605–614
- Edgington-Mitchell D (2019) Supersonic jet screech: half-century from Powell to the present. *Int J Aeroacoust* 18:118–188
- Edgington-Mitchell DM, Honnery DR, Soria J (2015) Multimodal instability in the weakly underexpanded elliptic jet. *AIAA J* 53:2739–2749
- Franquet E, Perrier V, Gibout S, Bruel P (2015) Free underexpanded jets in a quiescent medium: a review. *Prog Aerosp Sci* 77:25–53
- Greenberg PS, Klimek RB, Buchele DR (1995) Quantitative rainbow schlieren deflectometry. *Appl Opt* 34:3810–3825
- Ihme M (2017) Combustion and engine-core noise. *Annu Rev Fluid Mech* 49:277–310
- Kinzie KW, McLaughlin DK (1999) Aeroacoustic properties of supersonic elliptic jets. *J Fluid Mech* 395:1–28
- Kumar SMA, Rathakrishnan E (2016) Characteristics of a supersonic elliptic jet. *Aeronaut J* 120:495–519
- Love ES, Grigsby CE, Lee LP, Woodling MJ (1959) Experimental and theoretical studies of axisymmetric free jets, NASA TR, R-6
- McLachlan NW (1964) Theory and application of Mathieu functions. Dover, New York
- Menon N, Skews BW (2010) Shock wave configurations and flow structures in non-axisymmetric underexpanded sonic jets. *Shock Waves* 20:175–190
- Mitchell DM, Honnery DR, Soria J (2013) Near-field structure of underexpanded elliptic jets. *Exp Fluids* 54:1–13
- Rao AN, Kushari A, Mandal AC (2020) Screech characteristics of under-expanded high aspect ratio elliptic jet. *Phys Fluids* 32:076106
- Sakurai T, Handa T, Koike S, Mii K, Nakano A (2015) Study on the particle traceability in transonic and supersonic flows using molecular tagging velocimetry. *J Vis* 18:511–520
- Settles G (2001) Schlieren and shadowgraph techniques: visualizing phenomena in transparent media, 1st edn. Springer, Berlin
- Sugawara S, Nakao S, Miyazato Y, Ishino Y, Miki K (2020) Three-dimensional reconstruction of a microjet with a Mach disk by Mach-Zehnder interferometers. *J Fluid Mech* 893:A25
- Sugawara S, Nakao S, Miyazato Y, Ishino Y, Miki K (2021) Quantitative flow visualization of slightly underexpanded micro-jets by Mach-Zehnder interferometers. *Flow Turbul Combust* 106:971–992
- Takano H, Kamikihara D, Ono D, Nakao S, Yamamoto H, Miyazato Y (2016) Three-dimensional rainbow schlieren measurements in underexpanded sonic jets from axisymmetric convergent nozzles. *J Therm Sci* 25:78–83
- Tam CKW (1988) The Shock-cell structures and screech tone frequencies of rectangular and non-axisymmetric supersonic jets. *J Sound Vib* 121:135–147
- Wernet MP (2016) Application of tomo-PIV in a large-scale supersonic jet flow facility. *Exp Fluids* 57:1–24
- Yoon JH, Lee SJ (2003) Investigation of the near-field structure of an elliptic jet using stereoscopic particle image velocimetry. *Meas Sci Technol* 14:2034–2046
- Yüceil KB (2017) A comparison of PIV and interferometric Rayleigh scattering measurements in the near field of underexpanded sonic jets. *Aerosp Sci Technol* 67:31–40

Publisher's Note Springer Nature remains neutral with regard to jurisdictional claims in published maps and institutional affiliations.